

# James Webb Space Telescope: Characterization of Flight Candidate NIR InSb Arrays

Craig W. MCMurtry<sup>a</sup>, William J. Forrest<sup>a</sup>, Andrew C. Moore<sup>a,b</sup>, and Judith L. Pipher<sup>a</sup>

<sup>a</sup>University of Rochester, Rochester, NY, USA

<sup>b</sup>Rochester Institute of Technology, Rochester, NY, USA

## ABSTRACT

The James Webb Space Telescope (JWST), the successor to the Hubble Space Telescope, will draw on recent improvements in infrared array technologies to achieve its goals and mission. In order to best meet the goals of JWST, NASA is funding a competition between two near infrared detector technologies: InSb detector arrays from Raytheon Vision Systems and HgCdTe detector arrays from Rockwell Scientific. The University of Rochester, in collaboration with Raytheon, is testing near infrared InSb detectors in a 2048 x 2048 array format to meet the stringent requirements for JWST. Results from characterization under top level requirements, such as noise, quantum efficiency, well capacity, pixel operability, etc., are discussed. Dark current and its contribution to the total noise are analyzed.

This is a companion work to the paper in these SPIE proceedings by Alan Hoffman, Peter Love, and Joseph Rosbeck (Raytheon Vision Systems).<sup>1</sup>

**Keywords:** NIR, near infrared array detector, InSb, JWST, low noise, low dark current, high quantum efficiency

## 1. INTRODUCTION

The Infrared Astronomy group led by William Forrest and Judith Pipher at the University of Rochester (UR) is one of three independent detector testing laboratories for NASA's JWST.<sup>2,3</sup> The University of Rochester has achieved low noise, low dark current and high quantum efficiency, with good system electronics and optimized clocks and biases, using Raytheon produced high quality near infrared InSb array detectors which are ideal for space borne telescope missions, such as SIRTf.<sup>4,5,6,7,8,9,10,11,12,13,14</sup> We have chosen to work with Raytheon because InSb, on a suitably designed multiplexer, can meet or exceed all of the JWST requirements operating at a temperature of 30K. A detailed list of requirements and goals for JWST are provided by M<sup>c</sup>Creight *et al.*<sup>15</sup> and the University of Arizona's Request for Proposal.<sup>16</sup> The most relevant requirements and goals, as they pertain to this paper, are tabulated in the Summary Section (Section 3), along with results for InSb detectors from Raytheon. The omission of dark current as a requirement by M<sup>c</sup>Creight *et al.*<sup>15</sup> is not an over-sight, since the NASA JWST specifications focus on the total noise in 1000 seconds which includes any noise contribution from the dark current. However, the University of Arizona's Request for Proposal<sup>16</sup> does include a dark current requirement since it is vital to understand the total noise one would obtain for various integration times, not just 1000 seconds.

The near infrared detectors tested by the University of Rochester were provided by Raytheon Vision Systems (Raytheon). The NIR detectors are based on a 2048 × 2048 pixel format InSb detector bump-bonded to an SB-304 Read-Out Integrated Circuit which has 2 additional columns of 2048 reference pixels.<sup>1</sup> For the reader, we provide the following definitions and acronyms: Read-Out Integrated Circuit (ROIC) or bare multiplexer (mux), InSb Sensor Chip Assembly (SCA) which is an InSb detector bump-bonded to ROIC and Focal Plane Assembly (FPA) which is one or more SCAs housed and placed at a single image plane in an instrument.

Unless otherwise stated, all data were taken using Fowler sampling techniques,<sup>17</sup> where an N Fowler sample pair image is created by subtracting N averaged frame non-destructive read-outs at the beginning of integration

---

Further author information:

E-mail: craig.mcmurtry@rochester.edu or craig@astro.pas.rochester.edu

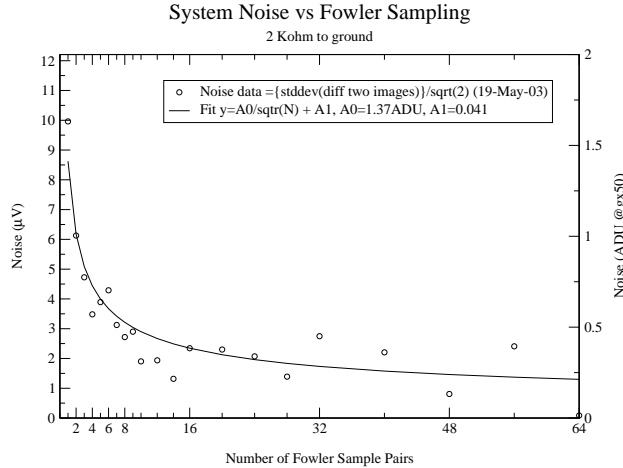


**Figure 1.** Plot of noise versus Fowler sample pairs ( $N$ ) for the UR system electronics with signal inputs shorted through a resistor which emulates the output characteristics of the Raytheon multiplexers. The overlaid fit uses  $y = A0/\sqrt{N}$ , where  $A0$  is the normalization/slope.

from  $N$  averaged frame non-destructive read-outs at the end of integration.<sup>10</sup> A second, common sampling read mode is sample-up-the-ramp (SUTR) where non-destructive reads are made at equally spaced time intervals during an integration and an optimal fit is made to the resultant data. For NASA’s JWST, the noise budget allocates a total of 10 electrons noise for the NIR array and controlling electronics, where  $9e^-$  noise is that allowed for the NIR array<sup>15</sup> using multiply sampled integrations, e.g. 8 Fowler sample pairs. For this reason, we have made a noise measurement of the University of Rochester system electronics using shorted inputs (see Figure 1). The University of Rochester system electronics signal chain uses differential amplifiers with input bandwidth limiting at 160 kHz from a single-pole RC filter prior to digitization. Although we have measured the University of Rochester system electronics’ noise, we do **not** subtract in quadrature the system noise from the total noise in any measurement. Thus the total noises quoted in this paper are real, achievable and reproducible results.

## 2. DATA

### 2.1. InSb SCA calibration

In order to obtain meaningful results, we needed to calibrate the InSb SCAs. This involved the measurement of source follower gain, capacitance, linearity and well depth (capacity). Unless otherwise stated, all measurements were obtained at 30.0K and an applied detector reverse bias of 300mV. The source follower gain of the SB-304 multiplexer is the product of gains from two series source follower FETs. The input voltage ( $V_{dduc}$ ) is varied while measuring output voltage ( $V_{out}$ ), see Figure 2. The pixel capacitance was measured using the variance versus signal method.<sup>18</sup> The linearity of the detector is plotted in Figure 3 which is obtained using a small flux and integrating over successively longer times until saturation is reached. The well depth or capacity is given by the saturating fluence level obtained at the largest integration times used in the above linearity measurement. The measured calibration values for both SCA 006 and SCA 008 are reported in Table 1. While it has been noted by Pain and Hancock<sup>19</sup> that, due to the inherent non-linear nature of photo-voltaic detectors, large errors can arise in both conversion gain (capacitance) and quantum efficiency, we do not follow their method of non-linear estimation. Instead, we have opted to follow a simpler method. We have indeed measured the capacitance at small signal levels and corrected all larger signal levels for such non-linearities as per the usual astronomical methods.<sup>20,21,22,23,24</sup> A more appropriate correction to conversion gain and quantum efficiency is detailed by

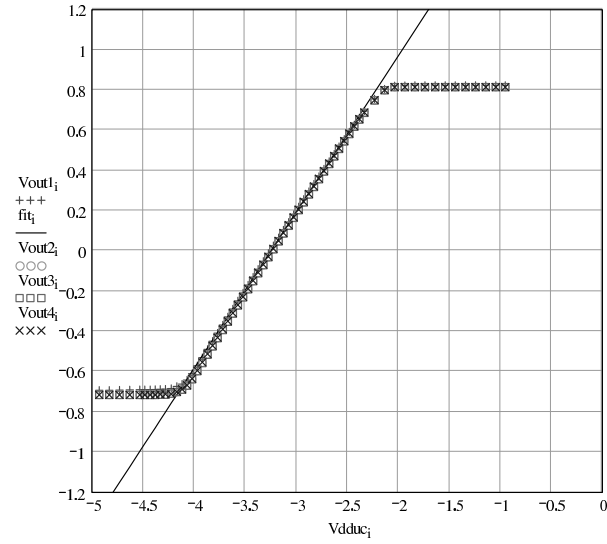


**Figure 2.** Plot of  $V_{out}$  versus  $V_{dduc}$  for SCA-006. The slope of the line fit is the source follower gain for the multiplexer.

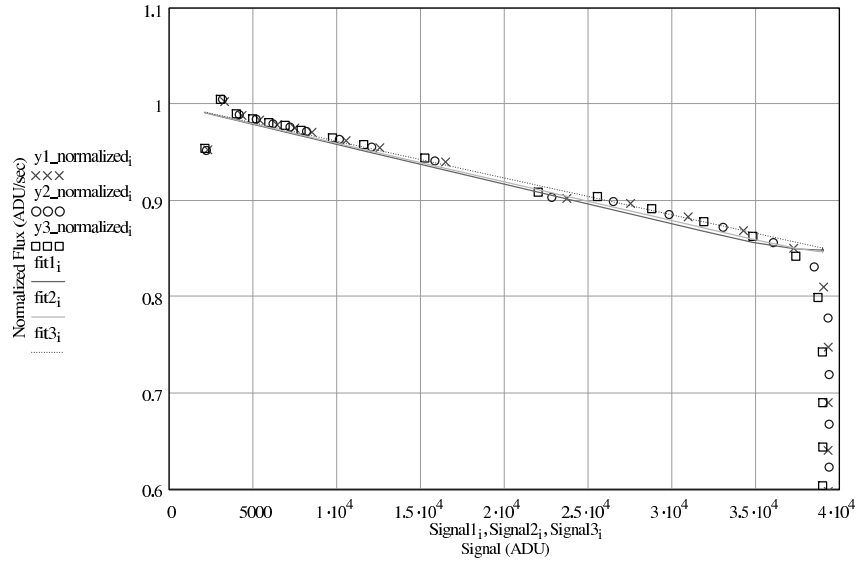


**Figure 3.** Plotted Signal Rate (normalized to unity) versus Signal ( $C_0/C$ ).

**Table 1.** Calibration numbers at 30.0K and applied detector reverse bias= 300mV.

SCA	Source Follower Gain	Capacitance (fF)	Capacitance ( $e^-/\mu V$ )	Well Depth ( $e^-$ )
006	0.777	66	0.68	$1.4 \times 10^5$
008	0.785	68	0.69	$1.3 \times 10^5$

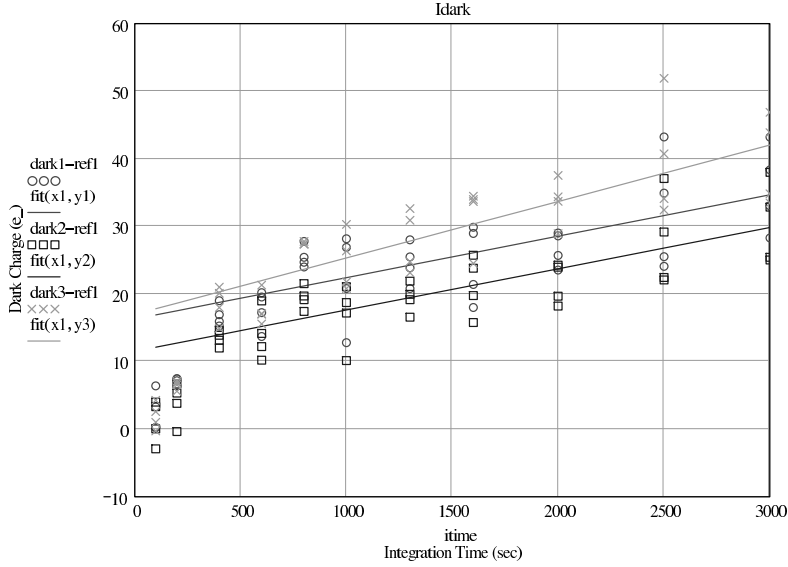


**Figure 4.** Dark charge versus integration time.

Moore,<sup>25</sup> although we have not yet applied his technique to our data. Moore estimates these corrections would reduce both the quantum efficiency and the noises reported here by  $\sim 8\%$  each.

## 2.2. Dark Current

Accurate, low dark current measurements are notoriously difficult due to light leaks and system instabilities. The use of reference pixels greatly aids in correcting the latter. After careful application of black paint and placement of light baffles, we have measured the light leak to be  $< 0.006e^-/s$  and may even be  $< 0.002e^-/s$  in the University of Rochester dewar. At temperatures near 30K, we have used three methods to measure the dark current: 1) dark charge versus integration time, 2) noise<sup>2</sup> versus integration time and 3) SUTR dark charge versus integration time. The three methods do not always agree.<sup>26</sup>

For the first method, dark charge versus integration time, multiple integration time dark exposures are taken, e.g. four dark exposures, employing Fowler-8 sampling, each at 100, 200, 400, 600, 800, 1000, 1300, 1600, 2000, 2500 and 3000 seconds integration time (see Figure 4). There is a dark charge-up at the short integrations which is consistent with previously seen dark charge-ups.<sup>26</sup> The use of reference pixels to subtract frame-to-frame drift due to slight temperature or bias fluctuations is vital to provide an accurate measurement of the dark current. The measured dark current at 30.0K using this method was  $0.010 e^-/s$  for SCA 006 and  $0.03 e^-/s$  for SCA 008.

The second method, noise<sup>2</sup> versus integration time, uses the exact same data set as the first with reference pixel corrections, except that now dark charge is replaced with noise<sup>2</sup> which is dominated by the noise in the dark charge (see Figure 5). The measured dark current at 30.0K was  $0.012 e^-/s$  for SCA 006 and  $0.025 e^-/s$  for SCA 008. The variation in dark current over the entire array of pixels is quite small. The number of pixels with dark current  $> 0.1e^-/s$  is 8736 or 0.21% for SCA 006 and 16104 or 0.38% for SCA 008. A sample dark current distribution for SCA 006 is shown in Figure 6.

The third method is similar to the first where dark charge versus integration time is plotted to obtain a dark current slope. However, this method employs a single dark exposure using the Sample-Up-The-Ramp (SUTR) technique (see Figure 7). While this method takes significantly less testing time, it does have the draw back of adding charge per read (sample) which can confuse the dark current measurement. The charge per read is  $0.09 e^-/read$  for SCA 006 and  $0.16 e^-/read$  for SCA 008. As we will show in Section 2.3, there is little to zero noise contribution due to the additional charge accumulated by large numbers of sampling.

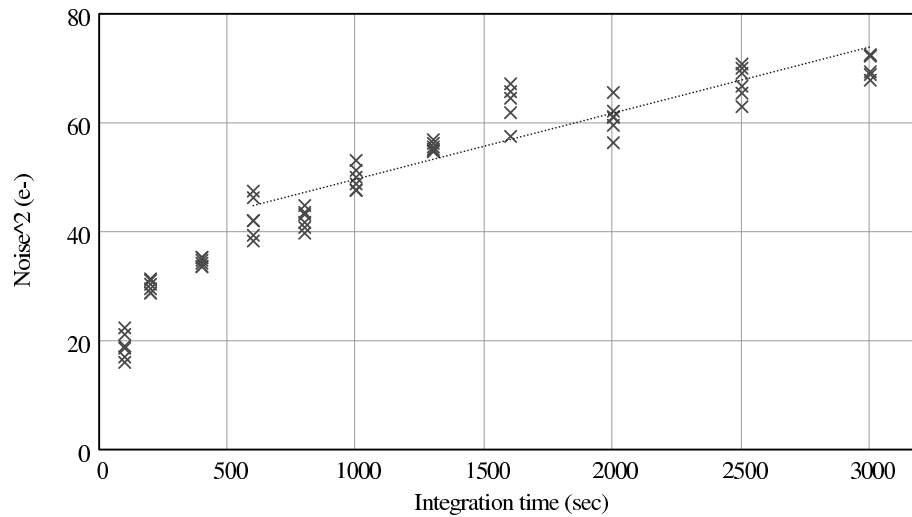


**Figure 5.** Noise<sup>2</sup> versus integration time for SCA 006. Above integration times of 500 seconds, the noise is dominated by the dark charge (due to dark current). This plot shows the total noise, i.e. no noise subtracted from the system or other sources. Notice that this device satisfies the JWST noise requirement of  $< 9e^-$  not just at 1000 seconds, but out to at least 3000 seconds.

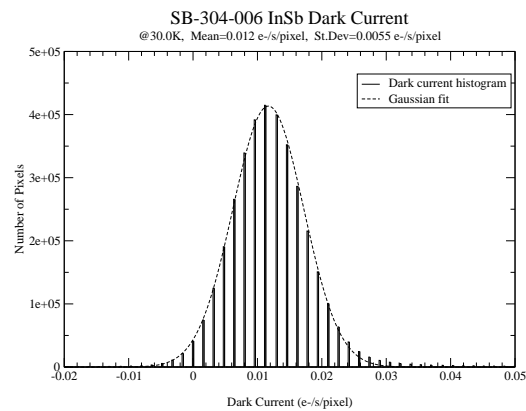


**Figure 6.** Dark current histogram for SCA 006. Out of  $2048^2$  pixels, only 8736 pixels have dark current  $> 0.1e^-/s$ .

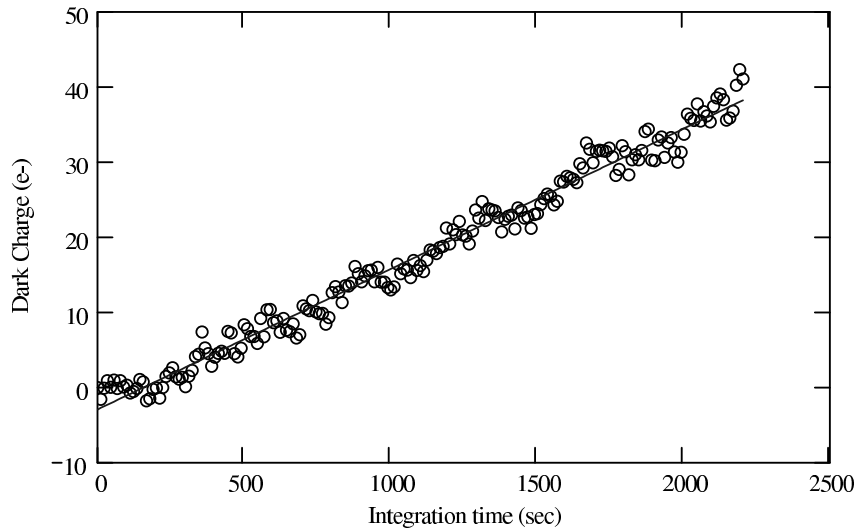


**Figure 7.** Dark charge versus integration time for SCA 006. The data were taken using SUTR mode with 200 samples spaced at 11.1 seconds. The data are corrected using reference pixels.

At temperatures above 35K, the dark current is larger and thus easier to measure. We allowed the dewar to run out of liquid helium which caused the detector to gradually rise in temperature. As the temperature slowly rose, we continually took dark exposures in order to measure the dark current. The resulting dark current data along with the above data take at stabilized temperatures are graphed in Arrhenius plots for both SCA 006 and SCA 008 (see Figure 8). For both SCAs the dark current does not follow the predicted dark current due to generation-recombination mechanisms. Similar departure from G-R dark current was seen in previous generation InSb detectors.<sup>26</sup> The possibility of surface currents due to non-ideal passivation will be investigated pending further funding for development. At 30.0K there was no detectable change in dark current with modest change in applied detector reverse bias (approximately 100mV change) for either SCA 006 or SCA 008. Therefore slightly larger well depths are possible with no adverse affect on dark current or noise.

Glow from sources related to the detector or multiplexer can also confuse the measurement of dark current. The first and most noticeable source of glow comes from photo-emissive defects (PEDs) which are caused by direct electrical shorts in the multiplexer. Raytheon has developed a technique to remove most of the PEDs from existing devices. Raytheon is actively pursuing foundry improvements to eliminate PEDs from future devices. Another possible glow can originate from the output amplifier on the multiplexer. SCA 006 showed no output amplifier glow, while SCA 008 did show a modest glow (approximately twice the dark current) that covered a quarter circular region 90 pixels in radius (center near pixel 1,1). The multiplexer used with SCA 008 has known small shorts which are likely the cause of the amplifier glow. A final source of glow can come from the digital circuitry of the multiplexer, namely the shift registers for row and column select. For both SCA 006 and 008, no measurable glow due to digital circuitry was detected.

### 2.3. Noise

The read noise was measured in regimes where the dark current makes little or zero contribution to the total noise, i.e. at sufficiently short integration times (see Figure 9). Both SCA 006 and SCA 008 demonstrated read noises that follow the predicted  $1/\sqrt{N}$  curve, where  $N$  is the number of Fowler sample pairs. For a single Fowler pair read, or a correlated double sample (CDS) read, SCA 006 provided  $12e^-$  of read noise, and SCA 008 provided  $14.5e^-$  of read noise. As can be seen by comparing Figures 1 and 9, the system noise (in  $\mu V$ ) is not the dominant noise contributor.

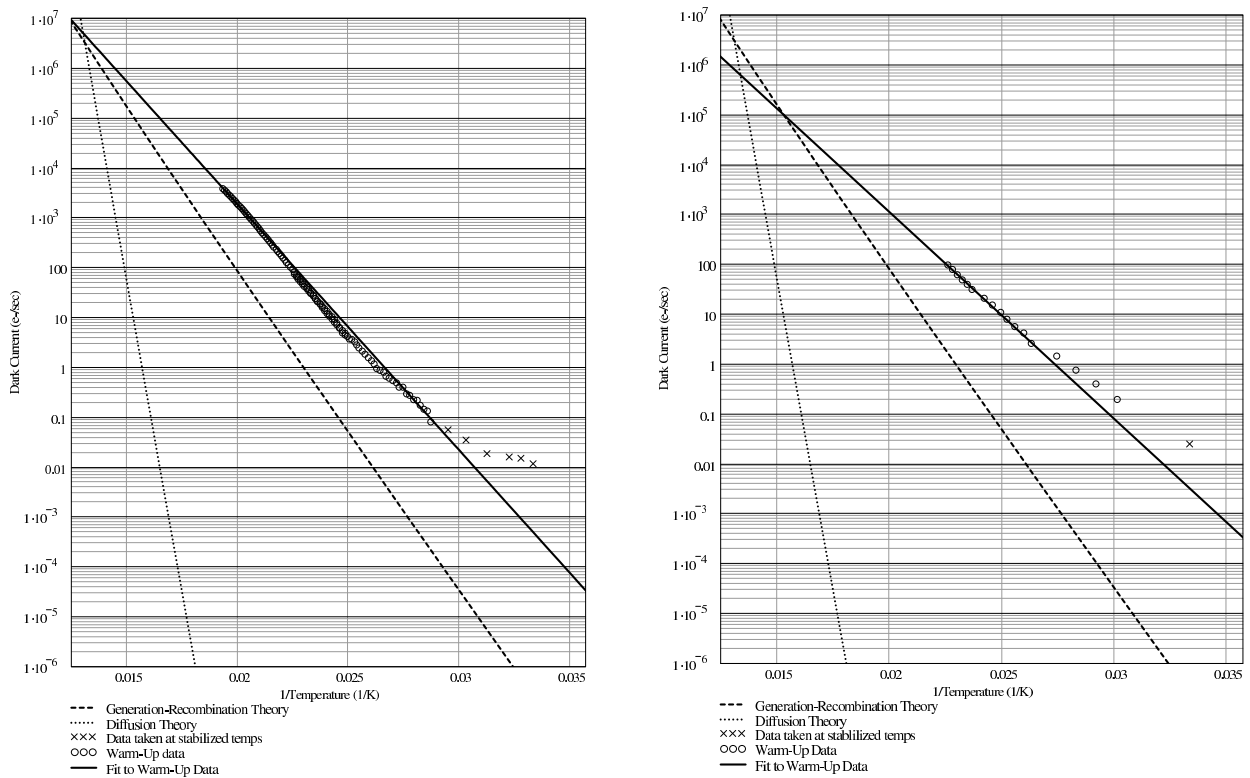


**Figure 8.** Dark current versus inverse temperature for SCA 006 (left) and SCA 008 (right) with theoretical plots of diffusion and generation-recombination dark currents for comparison.

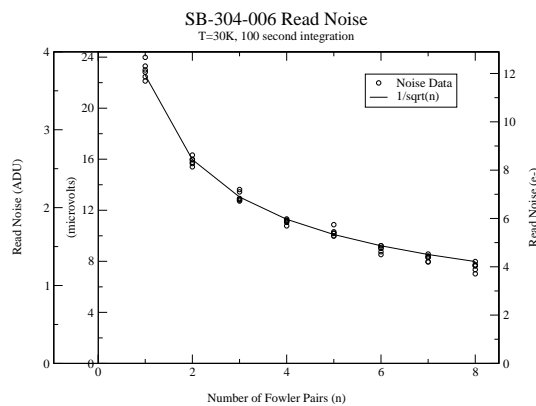


**Figure 9.** Graph of read noise versus number of Fowler sample pairs for SCA 006. The graph has three y-axes to facilitate easy conversion to the reader's favorite unit of measure. All data are taken at 30.0K with 100 seconds integration time so that dark current does not contribute to the noise. The data follow a  $1/\sqrt{N}$  curve.

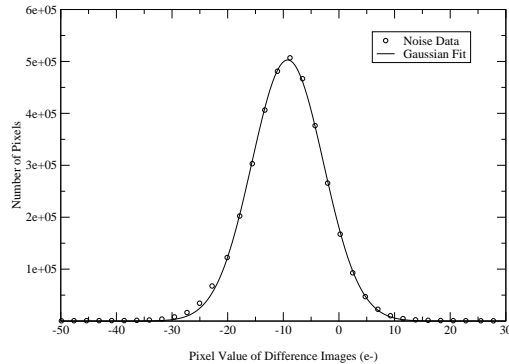


**Figure 10.** Gaussian fit to a histogram of pixel values from the difference of two 1000 seconds (divided by  $\sqrt{2}$ ), Fowler-8 sampled images. The FWHM is the noise per pixel. The average is a DC offset between the two images and does not affect the noise.

The measurement of total noise in 1000 seconds dark exposure was integral to the testing required by JWST. Again, several methods were employed to measure the total noise. In all cases, the noises quoted are the total noises and no attempt was made to remove noise from the system electronics, dark current or other sources. The first method computes standard deviations divided by  $\sqrt{2}$  of the pixel-to-pixel values within a rectangular region from the difference of two dark exposures. Cosmic ray hits are rejected using iterative  $4\sigma$  clipping. This method of box averages for noise measurements allows for more detailed spatial analysis on sub-array scales and is less computationally intensive for the test operator. For a  $50 \times 50$  pixel box size, the error in a given measurement is  $(\sqrt{50 \times 50})^{-1} = 2\%$ . In most cases, except near PEDs, the total noise measured using box averages was identical (within uncertainties) to the other full frame noise measurements below. Therefore, we will only report full frame noise measurements.

The second method involves making a Gaussian fit to a histogram of all of the pixels in a difference image divided by  $\sqrt{2}$  (see Figure 10). The standard deviation of the Gaussian is the noise per pixel, while the mean of the Gaussian is simply a DC offset between the two images. The Gaussian fit, by definition, rejects the cosmic ray hits. The measured total noise, in 1000 seconds Fowler-8 sample pairs, from this method is  $6.7e^-$  for SCA 006.

The final method for measuring the per pixel noise is the temporal noise measurement where the standard deviation of the mean is computed per pixel for a set of dark exposures (time series). The distribution is typically a Gaussian whose width depends on the number of images in the time series data set (see Figure 11). The time series data were taken using 25 Fowler-8 sampled 1000 seconds dark exposures. Since the standard deviation is computed per pixel over the time series, it is necessary to reject ( $4\sigma$  clipping) pixels that are affected by cosmic ray hits on a per image basis. The measured total noise, in 1000 seconds Fowler-8 sample pairs, from the temporal method is  $6.2e^-$  for SCA 006 and  $7.9e^-$  for SCA 008, both at 30.0K temperature.

As was mentioned in Section 2.2, there was no detectable noise contribution due to charge per read. The data used in the temporal noise measurement were actually Fowler-8 sample pair images reconstructed from the 98 samples of a SUTR series. From the dark current results, we deduced  $0.09e^-$  of dark charge per read. Thus, for the temporal noise measurement, one would expect  $(98 - 16) \times (0.09e^- / read)$  addition to the total noise power. However, the noise for the reconstructed Fowler-8 images of the temporal noise measurement was *less* than the noise measured in either of the other two methods (which used real Fowler-8 sample pair images), i.e. there was no measurable noise contribution due to this charge per read.

## 2.4. Quantum Efficiency

To accurately measure the quantum efficiency (QE), we used a dewar with the simplest possible optical path and therefore the simplest possible  $A\Omega$ . The optical path from the outside of the dewar to the detector consists

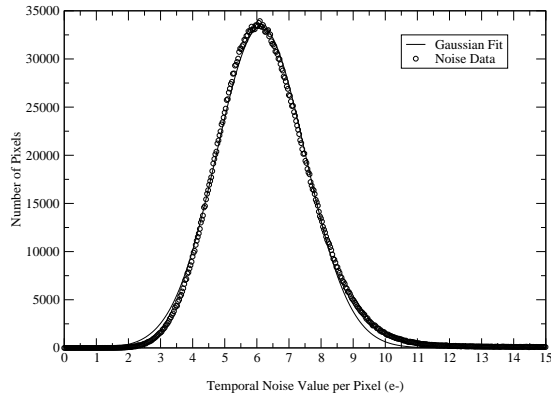


**Figure 11.** Gaussian fit to a histogram of noise per pixel from a time series of 25 Fowler-8 sampled 1000 seconds dark images (often referred to as a temporal noise measurement). The FWHM is the spread in noise per pixel. The average is the quoted temporal noise per pixel.

of 1) the dewar window, 2) liquid nitrogen shield, 3) liquid helium shield, 4) filter, and 5) circular aperture stop. The two cryogenic shields have circular openings that are sufficiently large such that they are well outside of the optical path. For flood illumination,  $A\Omega$  is therefore determined by the pixel area, aperture stop area and distance between the pixel and the aperture. The QE data were corrected for  $\cos^4 \theta$  effects. We corrected for photo-conductive gain at  $\lambda < 1.7\mu m$  by measuring the detective quantum efficiency. The responsive quantum efficiency (RQE) is given by:

$$RQE = \frac{S}{S_0}, \quad (1)$$

and detective quantum efficiency (DQE) by:

$$DQE = \frac{(\frac{S}{N})^2}{S_0}, \quad (2)$$

where  $S$  is the measured signal (in photons) from the detector,  $S_0$  is the actual signal (in photons, given by black body source, filter transmission and  $A\Omega$ ), and  $N$  is the noise obtained via the standard deviation of the difference of two signal measurements.

The cold IR filters in the University of Rochester dewar are all from OCLI or Barr and have transmission traces both at room temperature and at 77K. To measure the QE at  $\lambda > 3.0\mu m$ , the photon source used was a room temperature black body surface monitored with a calibrated temperature sensor. A liquid nitrogen cup was imaged to obtain the corrections to the BB emissivity and extra signal from dewar surfaces. For  $1.0\mu m < \lambda < 3.0\mu m$ , the QE was measured using a NIST calibrated black body (Omega BB-4A, 100 - 1000°C,  $\varepsilon = 0.99$ ). The cold visible filter is a KG-5 filter with transmission traces at room temperature and at 4.2K. For  $\lambda < 1.0\mu m$ , the QE was measured using a stabilized visible light source feeding an integrating sphere which in turn feeds a tunable liquid crystal filter and was monitored using a NIST calibrated Si diode detector. The results of RQE and DQE measurements are presented in Table 2. Since the DQE closely matches the expected value from the anti-reflective coating transmission curve (provided by Raytheon), we infer that the optical fill factor is  $> 98\%$ .

## 2.5. Image Latency

Image persistence or latency depends critically on the exact test procedure since the amount of latency depends upon the source flux, fluence and delays after exposure.<sup>27,28</sup> We present the results of image latency testing in Table 3. The image latency test protocols were developed based on past experience with SIRTf IRAC detector array testing and the science goals and observing environment (relatively bright field stars) of JWST. The delays

**Table 2.** Responsive Quantum Efficiency and Detective Quantum Efficiency given for various wavelengths.

SCA	$\lambda_c$	$0.65\mu m$	$0.70\mu m$	$1.255\mu m$	$1.645\mu m$	$2.19\mu m$	$3.81\mu m$	$4.667\mu m$	$4.892\mu m$
	$\Delta\lambda$	$0.04\mu m$	$0.05\mu m$	$0.298\mu m$	$0.332\mu m$	$0.41\mu m$	$0.63\mu m$	$0.176\mu m$	$0.422\mu m$
006	RQE	88%	105%	107%	96.2%	84.6%	97.1%	84.7%	80.1%
	DQE	82%	95%	97%	96.7%	85.3%	98.5%	85.0%	
008	RQE	114%			86.8%				
	DQE	97.1%							

**Table 3.** Image latency test protocols and results for InSb detectors.

Test #	Source Flux ( $e^-/s$ )	Source Exposure (s)	Source Fluence ( $e^-$ )	Delay (s)	Latent Integration Time (s)	Desired Latent Fluence	Measured Latent Fluence	SCA 006	SCA 008
1	300	100	30,000	30	100	0.03%	0.3%	0.12%	
2	300	100	30,000	1,000	100	0.003%	0.017%	0.01%	
3	30	1,000	30,000	30	1,000	0.015%			
4	300	500	150,000	30	100	0.06%	0.48%	0.22%	
5	300	500	150,000	1,000	100	0.006%	0.03%	0.01%	
6	3	10,000	30,000	200	8,000	< noise			
7	15	10,000	150,000	200	8,000	< noise			

were chosen based on telescope and instrument overhead. The results shown for SCA 006 do not employ any amelioration technique, while the results for SCA 008 employ an “autoflush” amelioration technique (developed by STScI<sup>3</sup>) which resets the detector array approximately once every second during the delay period (30-50 seconds).

## 2.6. Operability

We define the basic inoperability of an array to be those pixels which do not respond to light and/or are saturated within the minimum frame read time. The basic inoperability for SCA 006 and SCA 008 are shown in Figure 12. The basic inoperability for SCA 006 is 13.5%, and for SCA 008 is 1.94%. Most of the inoperable pixels in SCA 006 are unconnected pixels. SCA 006 represented an excellent first attempt at bonding large format InSb detectors to an SB-304 multiplexer, while SCA 008 shows a vast improvement in bonding the detector to the multiplexer.

## 2.7. Radiometric Stability

The radiometric stability of SCA 006 was measured using a method similar to RQE measurements at  $\lambda = 3.5\mu m$ . The “stable” source flux was a room temperature black body source, monitored via a calibrated temperature sensor. Most of the errors or uncertainties in this measurement are a result of the source calibration error or instabilities in the University of Rochester system electronics and not due the SCA itself. A series of integrations were taken over approximately a 9 hour period. SCA 006 exhibited instabilities < 0.07% standard deviation over 1000 seconds and < 0.19% over 32000 seconds. Further improvement by a factor of 10 to 100 in the measured radiometric stability could be achieved by using the University of Rochester’s NIST calibrated black body source at shorter wavelengths.

## 2.8. MTF and Electrical Cross-talk

We measured the modulated transfer function (MTF) using flood illumination incident on knife edges and circular apertures placed in contact with the InSb surface of an engineering grade device (SCA 009). Figure 13 illustrates the measured edge spread function at two wavelengths, J band  $1.25\mu m$ , and M’ band  $4.67\mu m$ . The edge spread

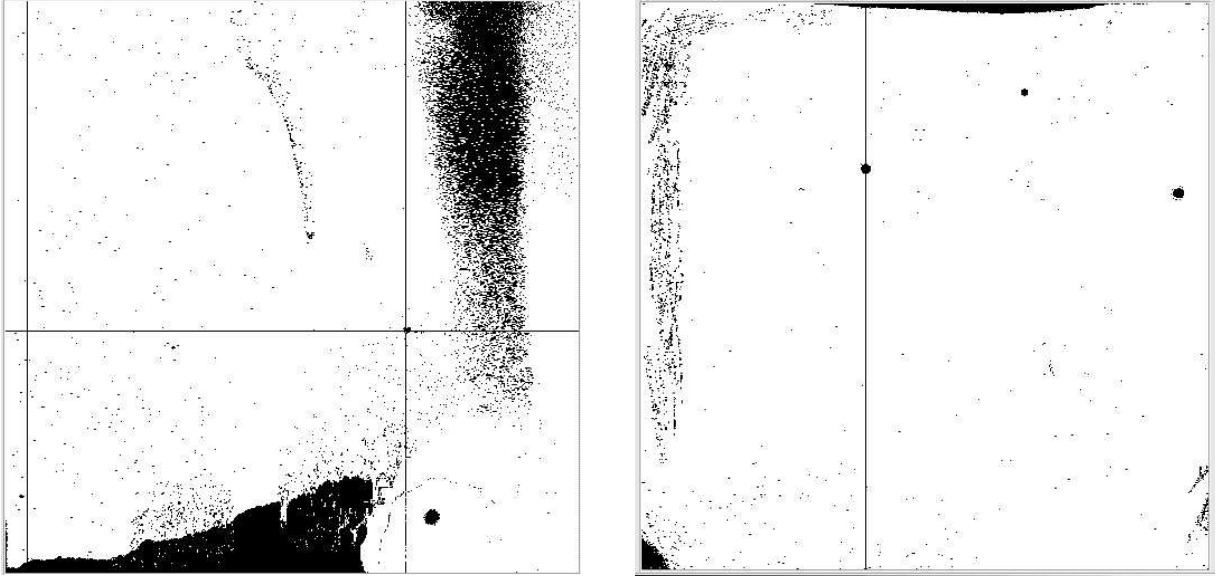


**Figure 12.** Operability of SCA 006 (left) and SCA 008 (right), where white represents operable pixels and black represents inoperable pixels. The basic inoperability of SCA 006 is 13.5%. The basic inoperability of SCA 008 is 1.94%. The small circular regions, two in SCA 006 and 3 in SCA 008, are PEDs. In SCA 008, the output amplifier glow (quarter circular region at lower left) is masked as inoperable even though the glow is slight (non-saturating).

function can be modeled by diffusion and the rectangular pixel function in terms of a parameter that is simply the ratio of (pixel pitch)/(thickness from absorbed photon to the depletion region). A best-fit model is shown in these figures where this ratio is 25/7. From the best fit model, the parameter  $\xi$  (frequency in cycles/thickness) can be determined, which then leads to the MTF<sup>29</sup>:

$$MTF = 0.64 \frac{2e^{-2\pi\xi}}{1 + e^{-4\pi\xi}} \quad (3)$$

where the factor 0.64 is the MTF at the critical Nyquist frequency for a perfect array detector. If we take the Nyquist frequency as 1/2(cycles/pixel pitch), then  $\xi = 7/50$  (cycles/thickness) and MTF=0.45. Alternatively, if we use 1/4(cycles/pixel pitch) as used by Rauscher,<sup>30</sup> then  $\xi = 7/100$  (cycles/thickness) and MTF=0.58.

The effects of cosmic ray hit spreading to neighboring pixels is characterized to obtain a quantitative result for pixel-to-pixel cross-talk. At the request of the University of Arizona,<sup>16</sup> we used multiple 1000 seconds dark exposures to find cosmic ray hits that were normal incidence, i.e. equal charge spreading to closest neighbor pixels. The four nearest neighboring pixels showed 0.5% – 1.2% cross-talk while the four next nearest neighbors showed < 0.1% cross-talk. Although this cross-talk satisfies the requirement of < 2%, it does not satisfy the requirement that < 10% of the pixels be above the noise requirement in 1000 seconds integration while in the presence of a cosmic ray flux of  $5\text{cm}^{-2}\text{s}^{-1}$ . Since that flux combined with the pixel pitch and format of the Raytheon InSb detectors leads to 3.125% of the pixels receiving a direct cosmic ray hit and 0.5% of a typical  $30,000e^-$  cosmic ray induced signal is above the noise requirement, then the Raytheon InSb detectors would typically have 5 pixels affected per normal incidence cosmic ray hit or 16% for the 1000 seconds integration. The number of pixels affected becomes worse for cosmic rays entering at other angles than normal incidence. The amount and placement of shielding for JWST may need to be re-evaluated.

In addition to nearest neighbor pixel cross-talk produced by charge diffusion in the bulk InSb detector, we characterized the electrical 4th pixel over cross-talk. The Raytheon SB-304 multiplexer uses four outputs that are interleaved, i.e. next pixel read by the same output channel is physically 4 pixels away on the detector array. The measured 4th pixel over cross-talk is 2%. However, the 4th pixel over cross-talk is deterministic and can be completely removed or corrected in software.

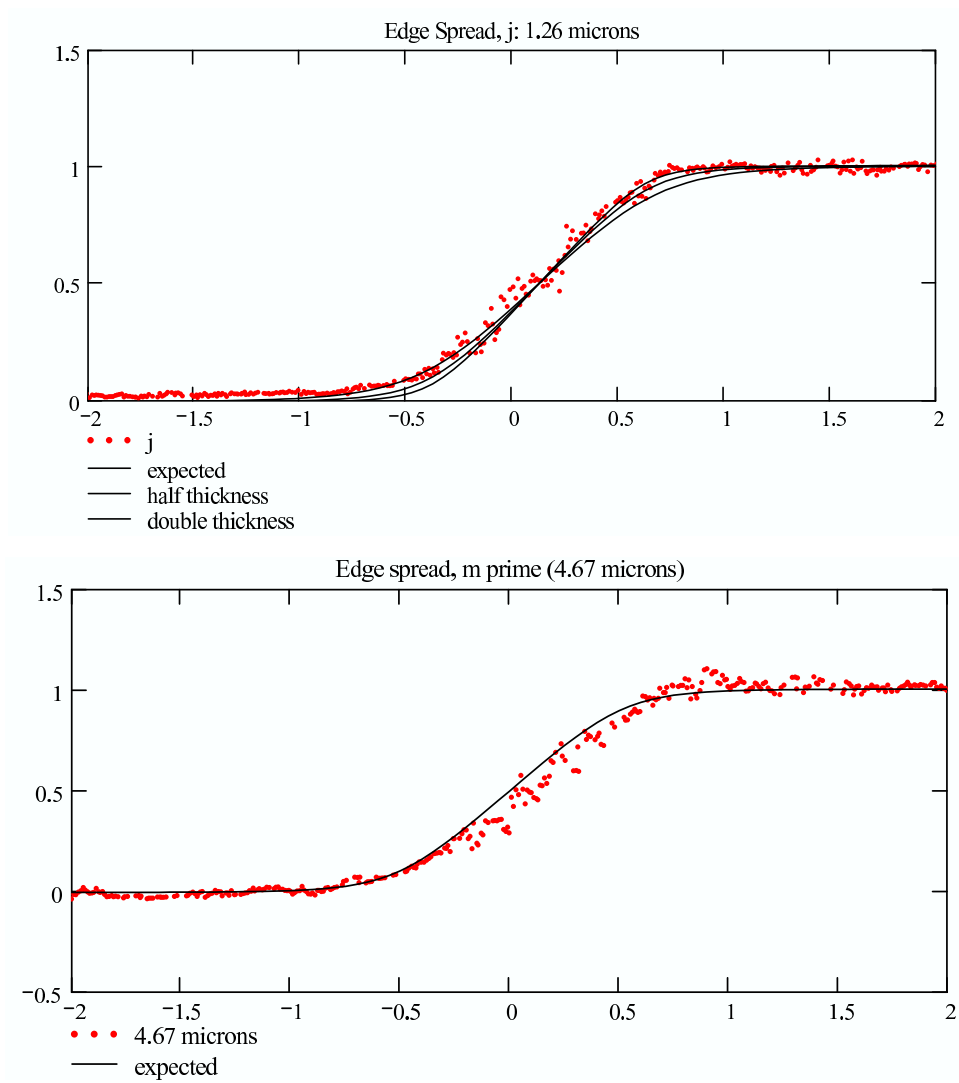


**Figure 13.** Edge spread functions represented by normalized intensity versus pixel position plots with overlaid fits at J band,  $1.25\mu m$ , (top) and M' band,  $4.67\mu m$  (bottom). The modeled parameter which is simply the ratio of the (pixel pitch)/(absorption distance from depletion region) is  $25/7$ . In the J band (top), the modeled parameter is also varied by twice and half of best fit to show the dependence on this parameter.

**Table 4.** JWST NIRCam FPA requirements and summary results for SCAs 006 and 008.

Parameter	Requirement	Goal	SCA 006 Result	SCA 008 Result
SCA Format	2048 × 2048 pixels		2048 × 2048 active pixels + 2 reference columns	2048 × 2048 active pixels + 2 reference columns
Fill Factor	> 95%	100%	> 98%	> 98%
Bad Rows/ Columns	< 5 containing > 1000 pixels		No	Yes
Bad Pixel Clustering	< 20 clusters up to 20 pixels		No	Yes
Pixel Operability	> 98%	> 99.5%	86.5% (basic)	98.1% (basic)
Total Noise in 1000 sec (Fowler-8 sampling)	≤ 9e <sup>-</sup>	≤ 2.5e <sup>-</sup>	6.2e <sup>-</sup>	7.9e <sup>-</sup>
Read Noise for single read	≤ 15e <sup>-</sup>	≤ 12e <sup>-</sup>	12e <sup>-</sup> (CDS)	14.5e <sup>-</sup> (CDS)
Dark current	≤ 0.01e <sup>-</sup> /s		0.012e <sup>-</sup> /s	0.025e <sup>-</sup> /s
DQE	70% for 0.6μm ≤ λ ≤ 1.0μm and 80% for 1.0μm ≤ λ ≤ 5.0μm	90% for 0.6μm ≤ λ ≤ 1.0μm and 95% for 1.0μm ≤ λ ≤ 5.0μm	82% 0.65μm 97% @ 1.25, 1.65, and 3.81μm	- 97% @ 1.25μm
Well Capacity	> 6 × 10 <sup>4</sup> e <sup>-</sup>	> 2 × 10 <sup>5</sup> e <sup>-</sup>	1.4 × 10 <sup>5</sup> e <sup>-</sup>	1.3 × 10 <sup>5</sup> e <sup>-</sup>
Electrical Cross-talk	< 5%	< 2%	< 1.3%	< 1.3%
Radiometric Stability	1% over 1000 sec		< 0.07%	< 0.07%
Latent Image	< 0.1% after 2nd read following > 80% full well exposure	0%	0.3%	0.12%
Frame Read Time	12 sec	< 12 sec	< 11 sec	< 11 sec
Pixel Read Rate	100KHz, 10μs/pix		100KHz, 10μs/pix	100KHz, 10μs/pix
Sub-Array Read	0.2s for 128 <sup>2</sup> pixels		< 0.05s	< 0.05s

### 3. SUMMARY AND CONCLUSIONS

Overall, the NIR InSb array detectors provided by Raytheon performed well in tests for the JWST requirements. The JWST NIRCam requirements and summary results for InSb SCAs 006 and 008 are presented in Table 4. Both the InSb detector arrays from Raytheon and the HgCdTe detectors arrays from Rockwell Scientific have demonstrated similar excellent performance. The University of Arizona has selected Rockwell Scientific to produce the NIRCam SCAs and FPAs, and the NIRSpc competition has yet to take place. We congratulate Rockwell Scientific and the University of Hawaii and look forward to equally beneficial, future detector competitions.

### ACKNOWLEDGMENTS

The authors would like to thank all the team members at Raytheon Vision Systems for their efforts to produce near infrared detector arrays that meet the JWST requirements and for their technical support during operation and testing. We would also like to thank the Independent Detector Test Lab at Space Telescope Science Institute

for their dedication to produce excellent results with both JWST flight candidate detector technologies from Raytheon Vision Systems and Rockwell Scientific in an extremely short time. Funding for this work was provided by NASA grant numbers: NAG-2975, NAG2-1142, NAG2-1280, NAG2-1452.

## REFERENCES

1. A. W. Hoffman, P. J. Love, and J. P. Rosbeck, "Mega-Pixel Detector Arrays: Visible to  $28\mu\text{m}$ ," in *Proc. SPIE, Focal Plane Arrays for Space Telescopes*, T. J. Grycewicz and C. R. McCreight, eds., **5167**, p. these proceedings, Aug. 2003.
2. W. J. Forrest, "Next Generation Space Telescope Instrument Technology Development," *Proposal to NASA NRA 00-OSS-03*, 2000.
3. D. F. Figer, B. Rauscher, M. W. Regan, J. Balleza, L. Bergeron, E. Morse, and H. S. Stockman, "Independent Testing of JWST Detector Prototypes," in *Proc. SPIE, Focal Plane Arrays for Space Telescopes*, T. J. Grycewicz and C. R. McCreight, eds., **5167**, p. these proceedings, Aug. 2003.
4. W. J. Forrest and J. L. Pipher, "Evaluation of a  $32 \times 32$  InSb CCD for use in Astronomy," in *NASA. Ames Research Center Proceedings of the Infrared Detector Technology Workshop*, C. R. McCreight, ed., Aug. 1983.
5. W. J. Forrest, A. Moneti, C. E. Woodward, J. L. Pipher, and A. Hoffman, "The New Near-Infrared Array Camera at the University of Rochester," *Publications of Astronomical Society of the Pacific* **97**, pp. 183–198, Feb. 1985.
6. W. J. Forrest and J. L. Pipher, "InSb arrays: Astronomy with a  $32 \times 32$  CCD/development of a  $58 \times 62$  DRO," in *NASA. Ames Research Center Proceedings of the Second Infrared Detector Technology Workshop 20 p (SEE N87-13704 05-35)*, C. R. McCreight, ed., Feb. 1986.
7. J. Wu, W. J. Forrest, J. L. Pipher, N. Lum, and A. Hoffman, "Development of infrared focal plane arrays for space," *Review of Scientific Instruments* **68**, pp. 3566–3578, Sept. 1997.
8. J. L. Hora, G. G. Fazio, S. P. Willner, M. L. Ashby, J. Huang, S. T. Megeath, J. R. Stauffer, E. V. Tollestrup, Z. Wang, W. J. Glaccum, J. L. Pipher, W. J. Forrest, C. R. McCreight, M. E. McKelvey, W. F. Hoffman, P. Eisenhardt, J. A. Surace, W. T. Reach, S. H. Moseley, R. G. Arendt, K. P. Stewart, and F. D. Robinson, "Calibration and performance of the infrared array camera (IRAC)," in *Proc. SPIE, Infrared Spaceborne Remote Sensing VIII*, M. Strojnik and B. F. Andresen, eds., **4131**, pp. 13–25, Nov. 2000.
9. W. J. Forrest, H. Chen, J. D. Garnett, S. L. Solomon, and J. L. Pipher, "Near-infrared arrays for SIRTf, the Space Infrared Telescope Facility," in *Proc. SPIE, Infrared Detectors and Instrumentation*, A. M. Fowler, ed., **1946**, pp. 18–24, Oct. 1993.
10. J. D. Garnett and W. J. Forrest, "Multiply sampled read-limited and background-limited noise performance," in *Proc. SPIE, Infrared Detectors and Instrumentation*, A. M. Fowler, ed., **1946**, pp. 395–404, Oct. 1993.
11. A. W. Hoffman, K. J. Ando, A. D. Estrada, J. D. Garnett, N. A. Lum, P. J. Love, J. P. Rosbeck, K. P. Sparkman, A. M. Fowler, J. L. Pipher, and W. J. Forrest, "Near IR arrays for ground-based and space-based astronomy," in *Proc. SPIE, Infrared Astronomical Instrumentation*, A. M. Fowler, ed., **3354**, pp. 24–29, Aug. 1998.
12. G. G. Fazio, J. L. Hora, S. P. Willner, J. R. Stauffer, M. L. Ashby, Z. Wang, E. V. Tollestrup, J. L. Pipher, W. J. Forrest, C. R. McCreight, S. H. Moseley, W. F. Hoffmann, P. Eisenhardt, and E. L. Wright, "Infrared array camera (IRAC) for the Space Infrared Telescope Facility (SIRTf)," in *Proc. SPIE, Infrared Astronomical Instrumentation*, A. M. Fowler, ed., **3354**, pp. 1024–1031, Aug. 1998.
13. J. L. Pipher, W. J. Forrest, and J. Wu, "InSb arrays for SIRTf," in *Proc. SPIE, Infrared Detectors and Instrumentation for Astronomy*, A. M. Fowler, ed., **2475**, pp. 428–434, June 1995.
14. R. D. Thom and B. T. Yang, "Low-background InSb array development," in *NASA. Ames Research Center Proceedings of the Second Infrared Detector Technology Workshop (SEE N87-13704 05-35)*, C. R. McCreight, ed., Feb. 1986.
15. C. McCreight, M. Greenhouse, D. Figer, R. Martineau, M. Jurotich, and B. Seery, "NGST ISIM Technology Development Requirements and Goals for NGST Detectors," <http://www.ngst.nasa.gov/doclist/bytitle.html> **Document 641**, 2001.

16. M. Rieke, E. Young, G. Rieke, K. Hodapp, and M. Fastje, "The University of Arizona Request for Proposal for James Webb Space Telescope NIRCам Focal Plane Arrays," <http://w3.arizona.edu/~pacs/purch/vendor/vendorrfp.htm> **RFP L090302**, 2003.
17. A. M. Fowler and I. Gatley, "Noise reduction strategy for hybrid IR focal-plane arrays," in *Proc. SPIE, Infrared Sensors: Detectors, Electronics, and Signal Processing*, T. S. Jayadev, ed., **1541**, pp. 127–133, Nov. 1991.
18. L. Mortara and A. Fowler, "Evaluations of CCD: Performance for Astronomical Use," *Proc. SPIE, Solid State Imagers for Astronomy* **290**, pp. 28–30, 1981.
19. B. Pain and B. Hancock, "Accurate Estimation of Conversion Gain and Quantum Efficiency in CMOS Imagers," in *Proc. SPIE, Sensors and Camera Systems for Scientific, Industrial, and Digital Photography Applications IV*, M. Blouke, N. Sampat, and R. Motta, eds., **5017**, pp. 94–103, Jan. 2003.
20. R. R. Joyce, "InSb Detectors for Ground-based Astronomy," in *Proc. SPIE, Infrared Detectors*, W. L. Wolfe, ed., **443**, pp. 50–58, Aug. 1983.
21. R. R. Joyce, "Observing with Infrared Arrays," in *Publications of ASP, Astronomical CCD Observing and Reduction Techniques*, S. B. Howell, ed., **23**, p. 258, Jan. 1992.
22. R. R. Joyce, A. M. Fowler, and G. B. Heim, "Astronomical longslit spectrograph utilizing a 256x256 InSb focal plane array," in *Proc. SPIE, Instrumentation in Astronomy VIII*, D. L. Crawford and E. R. Craine, eds., **2198**, pp. 725–735, Jan. 1994.
23. F. Lacombe, D. Tiphene, D. Rouan, P. Lena, and M. Combes, "Imagery with Infrared Arrays: I - Ground Based System and Astronomical Performances," *Astronomy and Astrophysics* **215**, pp. 211–217, May 1989.
24. C. G. Wynn-Williams and E. E. Becklin, "Infrared Astronomy with Arrays," in *Proc. of the Workshop on Ground-based Astronomical Observations with Infrared Array Detectors*, C. G. Wynn-Williams and E. E. Becklin, eds., Jan. 1987.
25. A. C. Moore, Z. Ninkov, and W. J. Forrest, "Interpixel Capacitance in Nondestructive Read-out Focal Plane Arrays," in *Proc. SPIE, Focal Plane Arrays for Space Telescopes*, T. J. Grycewicz and C. R. McCreight, eds., **5167**, p. these proceedings, Aug. 2003.
26. C. W. McMurtry, W. J. Forrest, A. C. Moore, and J. L. Pipher, "Next Generation Space Telescope: NIR InSb Array Development," in *Proc. SPIE, IR Space Telescopes and Instruments*, J. C. Mather, ed., **4850**, pp. 847–857, Aug. 2002.
27. S. L. Solomon, J. D. Garnett, and H. Chen, "Investigation of Charge Trapping Effects in InSb Focal Plane Arrays," in *Proc. SPIE, Infrared Detectors and Instrumentation*, A. M. Fowler, ed., **1946**, pp. 33–45, Aug. 1993.
28. R. G. Benson, W. J. Forrest, J. L. Pipher, W. J. Glaccum, and S. L. Solomon, "Spatial distributions of hole traps and image latency in InSb focal plane arrays," in *Proc. SPIE, Infrared Spaceborne Remote Sensing VIII*, M. Strojnik and B. F. Andresen, eds., **4131**, pp. 171–184, Nov. 2000.
29. A. C. Moore, *Theoretical and Practical System Aspects of Hybridized Array Control*. PhD thesis, Rochester Institute of Technology, work in progress.
30. B. Rauscher, "A Note on NGST Detector Modulation Transfer Function Guidelines," <http://www.ngst.nasa.gov/doclist/bytitle.html> **Document 662**, 2000.